Department of Precision and Microsystems Engineering

Measurement platform to characterize integrated photonic chips for fluid-based bio-sensing

Huaiyang Liu

Report no   : 2022.039
Coach   : Dr. Satadal Dutta
Professor   : Dr. Gerard J. Verbiest
Specialisation   : MNE & MSD
Type of report   : Master Thesis
Date   : 28 Jul 2022

TUDelft
Delft
University of
Technology

Abstract

Micro-ring resonators based on silicon-on-insulator (SOI) waveguide are widely used as sensors due to their small size and high sensitivities. After being fabricated on an integrated photonic technology, it can be applied in bio-chemical analyses crucial for human health monitoring, disease diagnoses, etc. In this project, we develop and construct a robust experimental setup based on the SOI based micro-ring resonator, which combines temperature control and modification of the waveguide cladding via surface treatments and microfluidic integration. The setup gives a controlled environment for characterizing the photonic chip under various chemical treatments or different physical ambient. After the setup is built, several experiments were performed to test the optical characteristics of the ring resonator, under different scenarios. These include temperature control, treatment of chip surface with sodium chloride and glucose solutions at varying concentrations, and lastly chip-surface functionalization for biomarker detection. With these experiments (also validated by numerical simulations), we demonstrate the robustness and reliability of our setup.

1 Introduction

Health monitoring is drawing more attention these days. As the number of patients with chronic diseases increases over years, an effective and wearable health alarm could have a large potential market. Some people also want to know the state of their bodies when they are doing sports, or even in daily life. These demands motivate the idea of wearable devices with continuous health monitoring functions.

The health monitor system can be designed in different ways. A non-invasive contact method is widely used these days, with the main idea being to capture the minor changes on the human skin through the optical sensors attached to the skin. The sensors look for the certain components, which are technically referred to as biomarkers, to gather information about the user's body condition. For instance, the electrolyte in sweat is one important biomarker that the sensor wants to detect, as it could signify the change in one's health conditions like hydration [13] [8] [11]. This can be done with a designed bio-receptor which can bind with the biomarker to be detected, thus we can quantify the health status by measuring the number of combined receptors.

To keep track of the biomarkers, an integrated photonics sensor could be an excellent candidate for its small size and high sensitivity. To do so, a photonic waveguide is functionalized with receptors, when the fluid (such as sweat, saliva, urine) interacts with the waveguide, the receptors are combined with the biomarkers, which consequently changes the optical properties of the waveguide. Light goes through the system and is monitored when it exits. Therefore, if changes happen to the receptors, the optical properties of the waveguide will be altered and the changes finally be reflected in the behavior of the laser between the inlet and outlet, as shown in Fig. 1.

It is important to identify the parameters that affect the result because these sensors are sensitive to the change the environment. The change of the cladding material of the waveguide is the main factor, which includes the change in the functional layer attached on the chip and the liquid/air environment around it. Furthermore, the temperature factor should also be considered because the refractive indices change with temperature.

This project focuses on the experimental setup for the photonic chips, building an environment for variable control and examination. This includes two different control systems: cladding control and temperature control. The first major component is a micro-fluidic channel to control the cladding of the waveguide. It should be able to make the liquid flow over certain area of the chip surface, and should not affect other structures on the chip. Second, we need a temperature control system that should be able to adjust the temperature of the experiment environment.
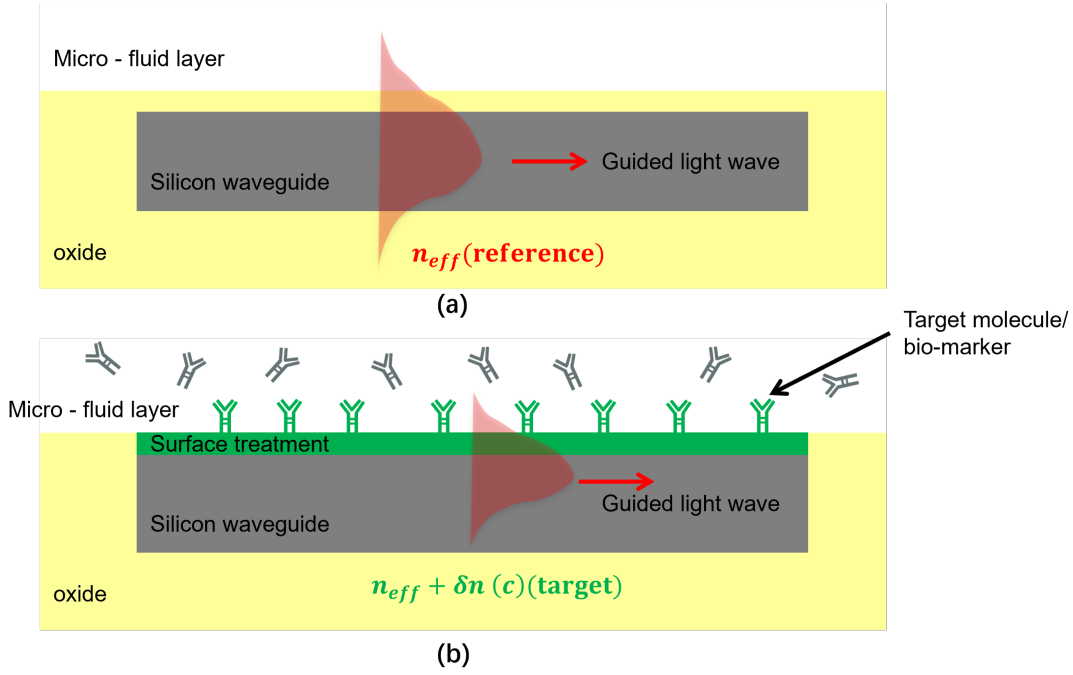
Figure 1: Sensing principle of the photonic waveguide with functional layer. (a) shows the guided wave transmitting through the silicon waveguide. (b) shows the detection of target molecule or biomarkers. The binding of the biomarker with the treated surface causes a change in effective refractive index of the structure and this is detected by the guided wave.

Also, to measure the laser light going through the chip, the supplementary alignment system and data collection devices are added to the setup. The framework of the setup is shown in Fig. 2.

After the setup is built, we run simulations of the photonic chip to predict the performance of the ring resonator. Similar to the design of experimental setup, the simulation also focuses on the cladding change and temperature change.

Finally, experiments are performed to check the characteristics of the chip with respect to several factors. The results are compared with the simulation and analysed following the methodology described in [9] and [15]. Although the setup is built for a particular chip structure, the idea can be easily altered and generalized to fit other chip designs. The manufacturing process of the setup is also easy to adjust.

The contribution of this project is two-fold:

- A generic robust photonic chip test setup is built and tested with a real chip.
- A photonic chip with functional layer on surface is measured with the change of surface condition, and the sensitivity of the chip as a sensor is calculated.
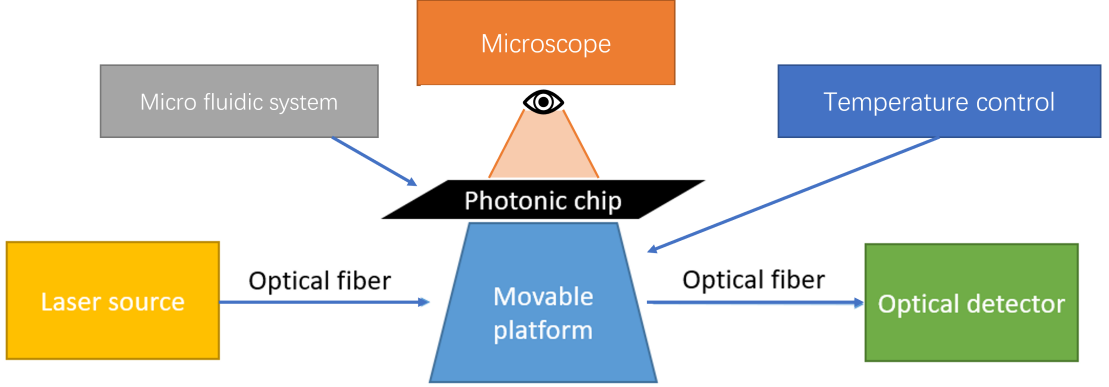
3

Figure 2: Framework of the experimental setup. Photonic chip is placed on a movable platform. The input and output light waves are transmitted through optical fibers and connected to the laser source and the optical detector. A microscope is placed to observe and align the chip with the fibers. A micro-fluidic system and temperature control system are added to the setup.
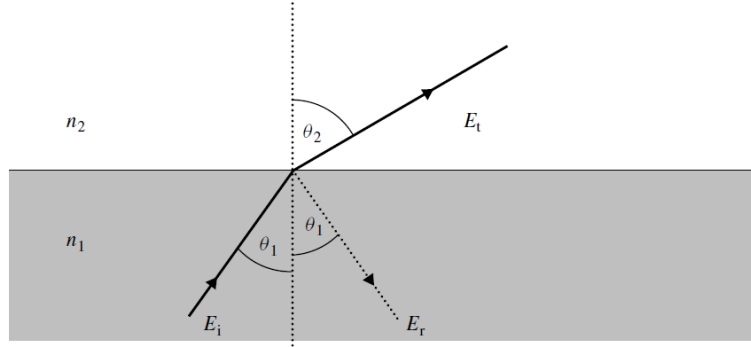

Figure 3: Snells law. Light incidents on an interface and splits into two beams. [9]

2   Background

In this section, we first introduce the physical and biological concepts that are related to the project. Then, we present the related works and state-of-the-art for this technology.
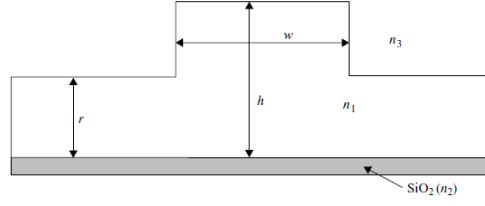
2.1   Waveguide

When light travels through the interface of two different mediums, refraction will happen and cause a deflection in angle. This relationship can be described with Snells Law [9], as shown in Equation 1 and in Fig. 3.

$$n_1 sin\theta_1 = n_2 sin\theta_2 \tag{1}$$

n is the refractive index of the medium, θ stands for the incidence angle. If the refractive index
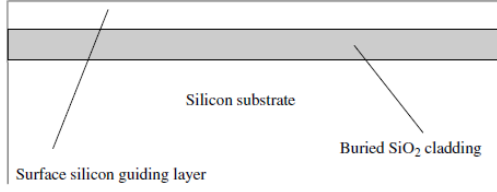
(a) A simple waveguide structure [9]

(b) A rib waveguide structure [9]

Figure 4: Different waveguide designs.

n_1 is larger than n_2, then as θ_1 increases, θ_2 will reach 90° and there will be no light coming out of medium 1, this is called total internal reflection (TIR). The angle of θ_1 is defined as critical angle θ_c shown in Eq. 2.

$$sin\theta_c = \frac{n_2}{n_1} \tag{2}$$

For incidence angles greater than this critical angle, no light is transmitted and TIR occurs. An optical waveguide is built based on this concept. Consider a sandwich structure as shown in Fig. 4a, the medium in the middle has a higher refractive index than the other parts. If the incidence angle light is properly chosen, TIR can happen in this medium so the light can be controlled and guided in a designed waveguide.

Note that the material for each part can be different, and the cross section geometry can also be in other shapes. A so called 'rib' waveguide is shown in Fig. 4b.

Light is an electromagnetic wave, the electric field E and magnetic field M associated with a propagating light can be described as Equation 3 and Equation 4, respectively, where z is the direction of propagation, E_0 and M_0 are the amplitude of electric and magnetic field, j is an imaginary number, k is the wave vector, t is time and ω is the frequency.

$$E = E_0 \exp[j(kz \pm \omega t)] \tag{3}$$
$$M = M_0 \exp[j(kz \pm \omega t)] \tag{4}$$

When the electromagnetic wave is traveling in space, the two fields are always perpendicular to each other. As shown in Fig. 5, the electric field is defined to oscillate in x-direction, then the magnetic field is always perpendicular to it as it lies in the y-direction.

The phase of the wave is

$$\phi = kz \pm \omega t \tag{5}$$

So the phase change rate along the propagation direction is

$$\frac{\partial \phi}{\partial z} = k \tag{6}$$

When light travels in the waveguide, the wave vector can be defined as Fig. 6, where k is the wave vector and can be mathematically expressed as
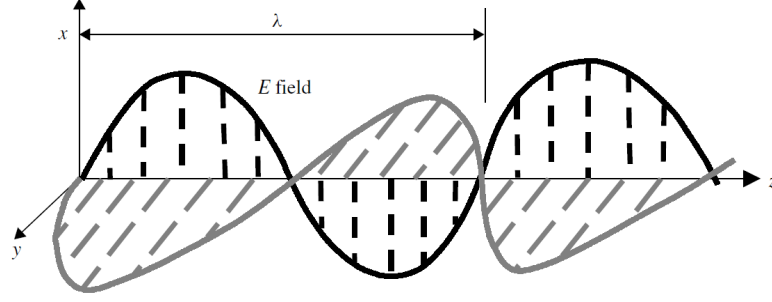
5

Figure 5: Electromagnetic wave in space. The E field and M field is perpendicular to each other. [9]

$$k = \frac{2\pi}{\lambda} \tag{7}$$

The y-direction vector is a standing wave when the wave completes a TIR, so it does a round trip with distance equal to multiples of the wavelength. If the wave vector is defined as Fig. 6, then the phase shift in y-direction can be introduced as Equation 8, where h is the thickness of the waveguide.

$$\phi_h = 2k_y h = 2k_0 n_1 h \cos\theta_1 \tag{8}$$

The phase shift of reflection on the interface can be defined as ϕ_u and ϕ_l, which is related to the refractive indices and incidence angle [9]. The total phase shift is

$$\phi_t = \phi_h - \phi_u - \phi_l \tag{9}$$

For it is a standing wave in y-direction,

$$\phi_t = \phi_h - \phi_u - \phi_l = 2n\pi \tag{10}$$

where n is an integer. Clearly, ϕ_t can be determined by θ_1 when the material properties remain constant. For different n values, there will be a series of discrete angles θ for them. This is called the mode of waveguide. Normally, the height of the waveguide is designed to be very low to make sure only the fundamental mode with only one θ can be chosen.
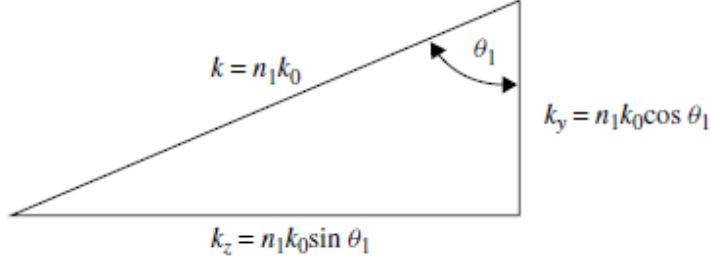
6

Figure 6: Wave vector definition. [9]

The component of z-direction k_z in Fig. 6 is defined with a parameter n_e, called the effective index of the mode, such that:

$$n_e = n_1 \sin \theta_1 \tag{11}$$

Then there is

$$k_z = n_e k_0 \tag{12}$$

The effective index is also a very important parameter for the measurement, with detailed information given in Sec. 2.2.

2.2 Ring Resonator & Optical Coupling

Ring resonator and optical coupler are the basic components of a silicon-on-insulator(SOI) waveguide system. As we discussed in Sec. 2.1 , the angle of incidence light needs to be adjusted to fit a certain value to match the mode , which can be realized using a coupler. As shown in Fig. 7, there are four mostly used couplers. All of them can couple light from outside to a waveguide.

Because an SOI waveguide system is usually on a flat chip, prism and grating coupling can be used. Considering the feasibility of manufacturing and also the form-factor and ease of chip assembly, a grating coupler will be used in this project. A sketch of the grating coupler and the optical fiber is shown in Fig. 9. This kind of structure is the entry and exit of the whole system, light will go into the chip from the input fiber and coupler and exit via a similar structure.

Another part of the SOI waveguide system is the micro ring resonator. In general, it consists of a loop and a coupling mechanism to access the loop [2]. When wave traveling in the loop finishes a round trip phase shift that numerically equals multiples of 2π, the waves interfere constructively and the cavity is in resonance. The resonance wavelength can be calculated as

$$\lambda_m = \frac{n_e L}{m} \tag{13}$$

where n_e is the effective index of the resonant mode, L is the cavity length and m is an integer which represents the number of loops in the ring.

Fig 9 shows two structures of ring resonators. The all-pass ring resonator is the simplest form that can be constructed from feeding one output of a directional coupler back into its input [2]. The
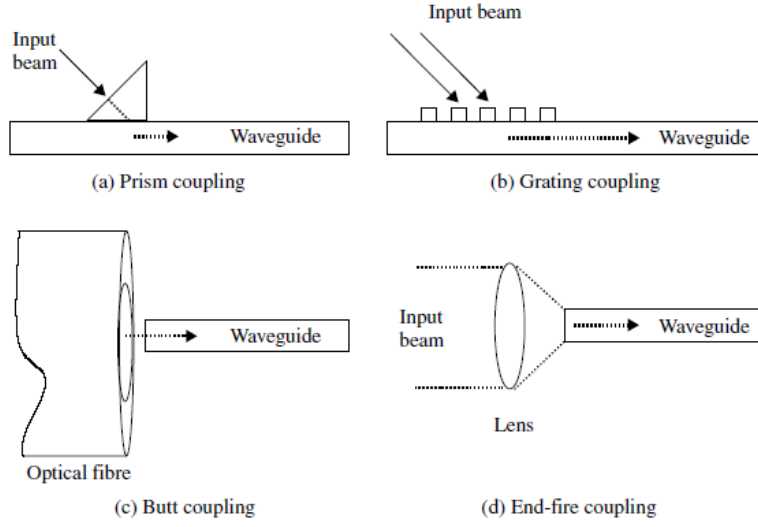
7

Figure 7: Sketches of four different couplers. (a) and (b) are often used in waveguides on a plane surface. (c) and (d) are often used when the input light source has the same direction with the waveguide. [9]
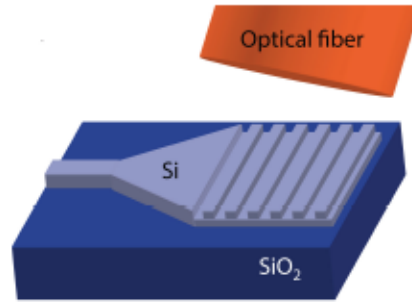

Figure 8: Grating coupler and optical fiber for incidence light. [15]

add-drop ring resonator is coupled to two waveguides, and the incident field is partly transmitted to the drop port.

It is clear that the change of effective index can cause a shift of resonance wavelength according to Equation 20. When the biomarkers bind with the bio-receptors, the index of the upper cladding in waveguide will change, and this process can be quantified by measuring the shift of the resonance wavelength.

2.3 Biological Sensing

Biomolecular detection technology plays a very important role in the functional part of this project. To detect certain component, a bio-receptor needs to be added onto the actuator, so that when the component in fluid passes through the actuator, the bio-receptor can bind with the actuator and cause a measurable change. These componets could be many substances that
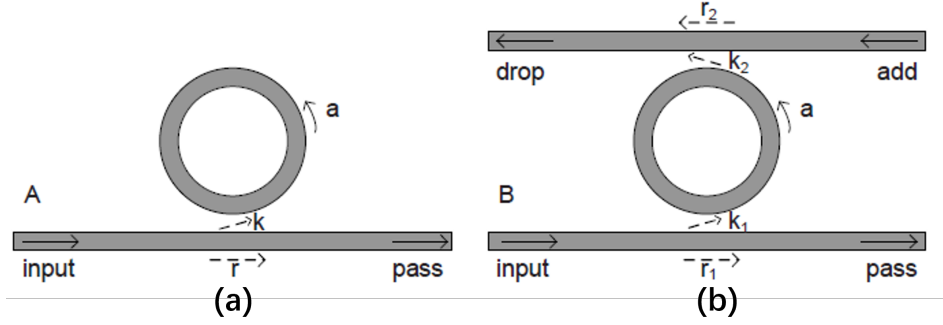
Figure 9: Two different structure of ring resonators. (a) All-pass ring resonator; (b) Add-drop ring resonator. For all-pass ring resonator, it can be constructed from feeding one output of a directional coupler back into its input. For Add-drop ring resonator, part of the incident field is transmitted to the drop port. [2]

include meaningful biological and chemical information, such as molecular, DNA, virus, etc. For example, Jonathan D. Suter et al. [13] demonstrated a method for quantitative real-time label-free detection of DNA sequences. A. Qavi et al. [8] also adopted the mechanism of tracking the biomarkers to successfully detect the microRNAs. Similarly, Ott Scheler et al. [11] used this process to develop a label-free biosensing method for transfer-messenger RNA (tmRNA). A picture illustrating this process is shown in Fig 10. Usually, these bio-receptors will be added to the surface of silicon photonic micro ring-resonators.
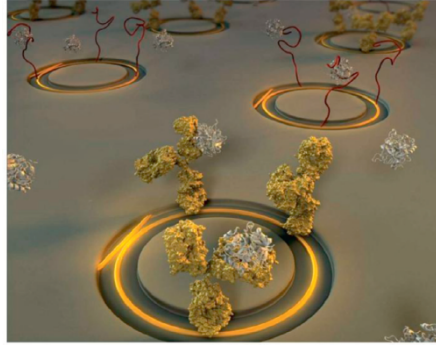

Figure 10: An artistic rendering of bio-receptor binding with biomarker. [4]

2.4 State-of-the-art

There are a lot of works in this field that inspired this project. Penades et al. [7] proposed a new type of mid-infrared SOI waveguide where the waveguide comprised a sub-wavelength lattice of holes acting as lateral cladding while at the same time allowing for the bottom oxide (BOX) removal by etching. Katrien De Vos et al. [3] introduced the process of coating and manufacturing of the chemical layer for the biosensor for monitoring real time interaction kinetics and high throughput screening of complex samples. They also build a completed biosensor platform as shown in Fig. 11. A micro-fluidic channel is applied on an array of ring resonator sensors. The
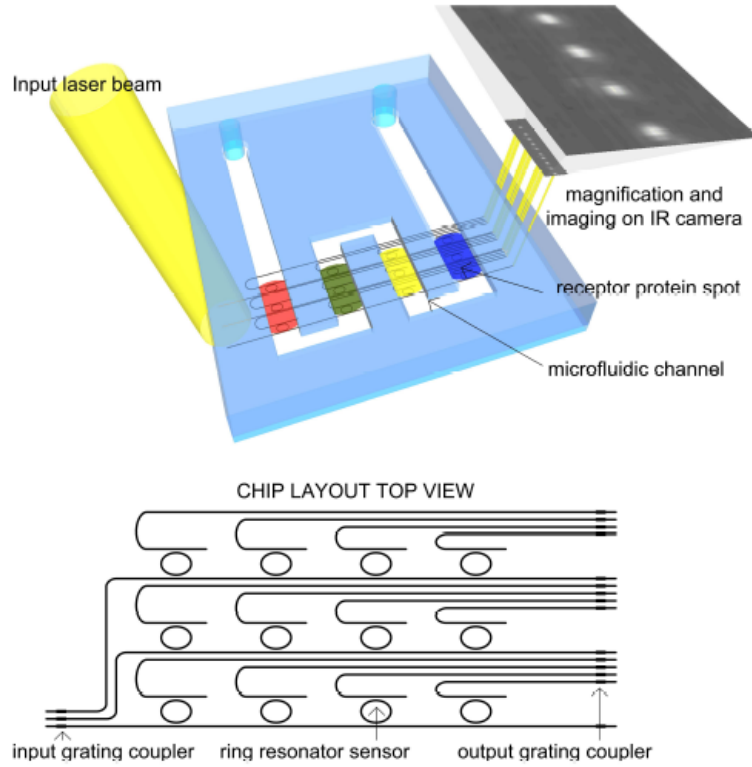
9

Figure 11: Illustration of biosensor platform. [3]

input laser beam transmits through the sensor array and gets magnified and detected by an IR camera. Sun et al. [12] designed a silicon concentric dual-microring resonator for refractive index sensing with optimization process.

As for the thermo-optical effect, in the work of Xu et al. [16], a new method of a real-time temperature shift cancellation sensor array was introduced, which was a interesting and workable way to counter the thermo-optical effect. And Rouger et al. [10] designed a detailed numerical modeling method for thermo-optical tuning for optical resonators and analysis. Chen et al. [1] built a highly-sensitive optical biosensor based on cascaded double-microring resonators where the sensor was integrated with microfluidic channels and investigated with its label-free detection capability. Wang et al. [14] introduced a new type of microfluidic channel design with ultralow-loss waveguide crossings. The waveguide crossings and all other on-chip passive-waveguide components were fabricated in one step with no additional planarization steps, which eliminated any orifices and led to leak-free fluid flow, as shown in Fig. 12.

In other people's work, there are already a lot of effort to control the temperature and fluidic environment of the photonic chip. Different from their work, this project focus on a general solution for all kind of SOI waveguide chip. The temperature control system in this project is simple and efficient to stabilize the temperature and avoid the influence of the thermo-optical effect. Also, the micro-fluidic system is simple structure with 3D-printed body and PDMS sheet,
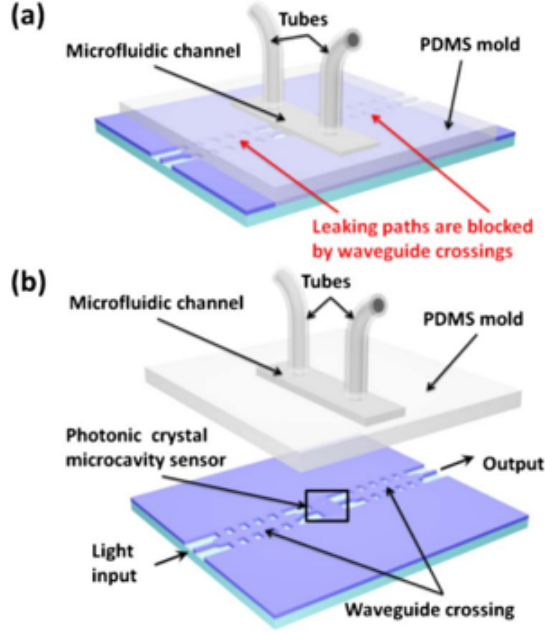
Figure 12: A microfluidic channel design shown in (a) 3D schematic of the integrated device and (b) the exploded view. The micro-fluidic channel is buried in the PDMS mold and attached on the waveguide. The structure of the waveguide seals liquid. The photonic crystal microcavity sensor is placed under the channel. [14]

which should be able to fit other kind of chip structure design easily. The manufacturing and the assembly process is also relatively simple, which make the reproduction of more setup very easy.

3   Simulation Process

In this project, a simulation of the SOI waveguide is necessary to validate the experimental result. With the software RSoft, the effective indices of the waveguide under different conditions can be obtained. After that, some important parameters such as resonance wavelength can be calculated with Matlab as the reference for the experiment process. In this section, the simulation and calculation are shown and discussed as the foundation of further experiments.

3.1   RSoft Simulation

The key parameter of the waveguide is the effective index, which determines all other important parameters such as resonance wavelength. In order to design the SOI waveguide that gives the desired properties, it is vital to first simulate the effective index under different physical conditions and waveguide geometries.

First, we define the waveguide cross section, which involves setting the material and the geometry of each part. The base material is silicon dioxide (SiO_2) and the waveguide material is silicon (Si). The width of the waveguide is 450nm and the height is 220nm. The waveguide is modeled
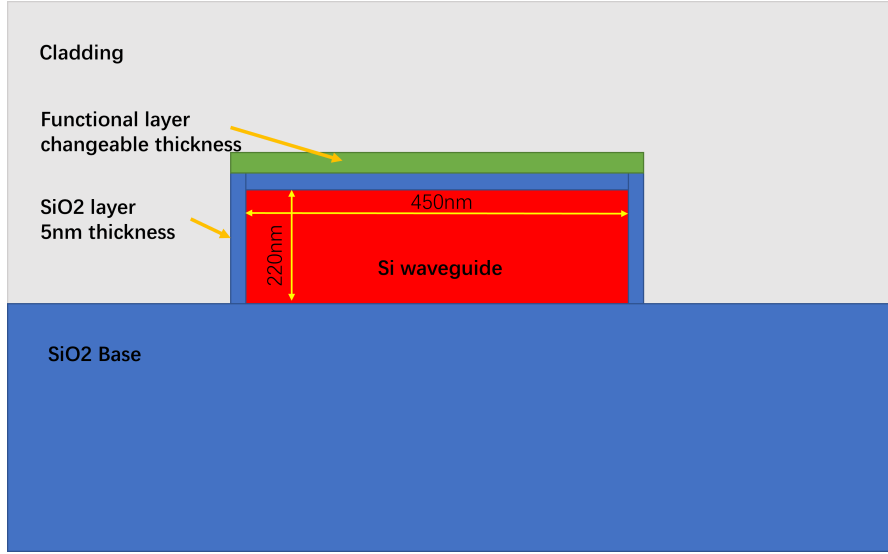
Figure 13: A sketch of the cross section of the waveguide in the simulation process.
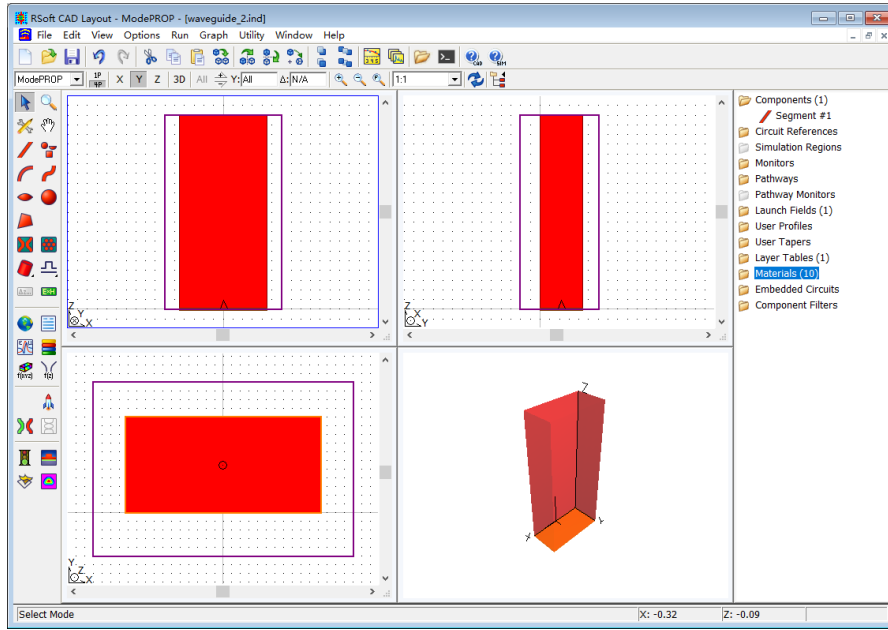

Figure 14: Simulation software RSoft interface. Three views and the 3D view of the waveguide are shown in four windows.

as covered by a (SiO_2) layer of 5nm. We use different cladding materials, or different surface functional layer thickness, during the simulation process, then the ideal refractive indices are set according to the material selection. A sketch of the cross section is shown in Fig. 13. Last, we define detailed geometry parameters of each material in the simulator. The interface of the software is shown in Fig. 14.

After setting up the cross section, we define the input field. In our setup, an electromagnetic field with 1550nm wavelength in transverse electric (TE) mode is induced to the cross section. Running the simulation with proper detecting window then gives the effective indices of this cross section.

In addition, we need to account for the dispersion effect in the simulation since it affects the light transmission, and in the end changes the refractive index computation result. The error caused by dispersion can be calculated from the change rate of the effective refractive index around the center wavelength 1550µm.

Different cladding simulation. Since we are interested in the change of the chip performance when its cladding material changes. By changing the cladding refractive index, we can simulate the effective refractive indices under different cladding environments.

Air is set as the default cladding material. The simulation also includes solution of glucose and sodium chloride with different concentration, with the refractive indices computed following Equation. 14 for glucose and Equation. 15 for sodium chloride.

$$n_{glucose} = 1.33 + 0.143C \ [6] \tag{14}$$

$$n_{NaCl} = 1.33 + 0.17151C \ [2] \tag{15}$$

Where 1.33 is the refractive index of water, and C is the concentration in mass %.

Temperature simulation The thermo-optical effect, which causes the refractive index to change with temperature, is critical for the effective refractive index. To simulate the change of effective refractive index with respect to temperature, we include the thermo-optical coefficient of silicon and silicon dioxide:

$$n_{Si} = 3.48 + 1.8 \times 10^{-4} \times (T - 300K) \ [5] \tag{16}$$

$$n_{SiO_2} = 1.44 + 8.5 \times 10^{-6} \times (T - 300K) \ [5] \tag{17}$$

With 3.48 and 1.44 as the refractive index of silicon and silicon dioxide at 300K, 1550nm, and T as the temperature in K.

Biomarker layer simulation. Since the thickness of the biomarker receptor layer is a design variable, different conditions should be simulated as well. There are four different surface conditions: bare chip with air cladding, chip with monolayer (hydrocarbons), chip with monolayer and antibodies (trastuzumab), and chip with monolayer after antibodies are removed. As shown in Fig. 15.

In simulation, different surface conditions are modeled as different thicknesses. The refractive index of the surface is 1.46. For the bare chip with air cladding, we consider the thickness to be 0nm. The chip with monolayer is 1.1nm thick. The chip with monolayer and antibodies is 7.4nm, and the chip with monolayer after antibodies are removed is 1.9nm. By changing the thickness in the geometry parameter, we can simulate the effective refractive indices under different bonding situations.

(a) Bare chip   (b) Chip with monolayer   (c) Chip with monolayer + antibody   (d) Chip with monolayer - antibody
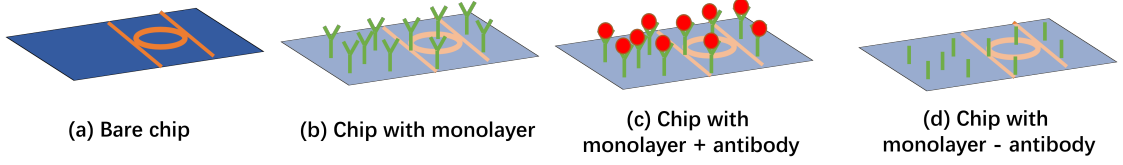
Figure 15: Different chip surface conditions. (a) is the bare chip, considered as air cladding. (b) is the chip after treated with monolayer attachment. (c) shows the chip with monolayer attached with antibodies, and (d) shows the chip with monolayer after antibodies are removed.

3.2   Analytical modeling of ring resonator

After obtaining the effective indices in RSoft, the model can be built in Matlab based on these results. Other important parameters in the model, such as group indices and resonance wavelengths are calculated to characterize the optical waveguide. Finally, the simulation outputs the sensitivity of resonance wavelength with respect to other variables.

Group index. The group index is computed with the effective indices around the input wavelength. It can be calculated using Equation 18.

$$n_g = n_e - \lambda \frac{\partial n_e}{\partial \lambda} \tag{18}$$

With $\frac{\partial n_e}{\partial \lambda}$ can be calculated as:

$$\frac{\partial n_e}{\partial \lambda} = \frac{n_e(1551nm) - n_e(1549nm)}{2} \tag{19}$$

Resonance wavelength. The resonance wavelength of the ring resonator is determined by both the effective index and the perimeter of the ring L, as shown in Equation 20.

$$m \cdot \lambda_m = n_e \cdot L \tag{20}$$

Where m is an integer indicating the order of resonance. By selecting m, make λ_m near the input wavelength 1550nm, we can calculate the resonance wavelength with first order dispersion, see Equation 21.

$$n_e = n_e(1550nm) + \frac{\partial n_e}{\partial \lambda}(\lambda_m - 1550nm) \tag{21}$$

Sensitivity. With the resonance wavelength at zero state (when layer thickness set to zero) and the group index, the sensitivity of resonance wavelength with respect to the layer thickness can be calculated with Equation 22.

$$\frac{\partial \lambda_m}{\partial \chi} = \left(\frac{n_e}{n_g}\right)\left(\frac{\lambda_c}{n_e}\frac{\partial n_e}{\partial \chi} + \frac{\lambda_c}{l}\frac{\partial l}{\partial \chi}\right) \tag{22}$$

The variable χ represents any factor that affect the resonance wavelength. λ_c is the resonance wavelength at zero state. When χ is the layer thickness, the partial derivative of perimeter l about χ becomes zero, thus Equation 22 can be rewritten as Equation 23.

$$\frac{\partial \lambda_m}{\partial \chi} = \frac{\lambda_c}{n_g}\frac{\partial n_e}{\partial \chi} \tag{23}$$

When χ is temperature, because the thermo-expansion coefficient is relatively small, we can also ignore the change of l near the room temperature. The sensitivity equation is also Eq. 23.

14

4 Experimental Setup

In this section, we introduce the experimental setup including the chip holder, the micro-fluidic system, the temperature control system and the measurement setup.

4.1 Chip holder and fiber alignment

The functionality of a chip holder is three-fold. First, it can hold the micro-fluidic channel and fix it with the test chip. Second, it is attached to a temperature control system that allows us to perform the temperature control experiment. Lastly, it aligns the chip with the optical fibers so that the laser source and photo-receiver can be connected.

The chip holder is designed with two layers. The bottom block is fixed on a 2-DoF stage which can rotate and move in y axis. The upper block is manufactured into a thin plate with both sides well polished, so that the heat transfer is more efficient. Three pairs of threaded holes are distributed evenly on the plate, these are fixing points of the micro-fluidic system.

The input and output optical fiber are fixed on two tilted plate with about 10 degrees with respect to the vertical axis. This angle is designed due to optimal in and out coupling efficiencies of the grating couplers on the chip. The plates holding the fibers are fixed on two three axis stage, providing a high precision manual x-y-z positioning. All these stages are mounted on the optical table to be isolated from oscillation.

When the chip is placed on the holder plate, the alignment of the optical couplers and the fibers will be performed under a microscopy camera. The camera is mounted on a three-axis stage and placed just above the chip holder. By connecting the camera to a laptop, the real time alignment can be done safely with the laser source on. The setup is shown in Fig. 16.

4.2 Micro-fluidic System

The micro-fluidic system in this setup is designed for two purposes. First is to seal in a small amount of liquid, so that it can form a cladding on the micro ring resonator. Second is to guide a continuous flow over the chip, with the help of tube and syringe pump.

As shown in Fig. 17, the ring resonators are distributed in the middle area, the input and output couplers are on both sides. Because the coupling of light require the optical fibers, the coupler area must not be covered. And the fluid channel should cover all the ring resonators on the chip so that all devices can be tested at the same time.

There are multiple choices for the micro-fluidic channel design. The method Wang et al. [14] uses is the combination of Polydimethylsiloxane (PDMS) block and arcylic clamp, as shown in Fig. 18.

This method can be applied easily because of the simple structure, yet there are also several problems to be noticed. First, the acrylic clamp force needs to be well balanced so that the liquid can be sealed in the channel properly. Second, the fabrication of the PDMS block needs to be handled carefully, and the design of the mold for PDMS block should consider the demoulding process. Furthermore, because the distance between the ring resonator area and the couplers area is narrow, the wall thickness of the channel must be constrained. Considering these factors, we experiment the solution with similar structure as shown in Fig. 19a and Fig. 19b.

Katrien De Vos et al. [3] shows a design using arcylic material fabricated with laser photoablation. Dimensions of the channels are 320x65 µm, as shown in Fig. 20. This solution is highly flexible
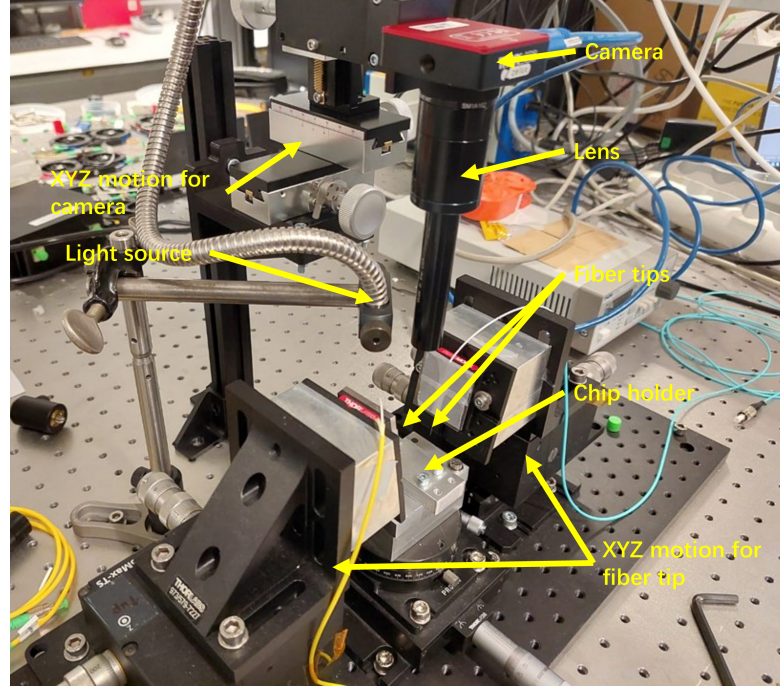
Figure 16: Alignment system and chip holder. Chip is placed on the chip holder and aligned with the fiber tips under the camera with the help of the XYZ motion.
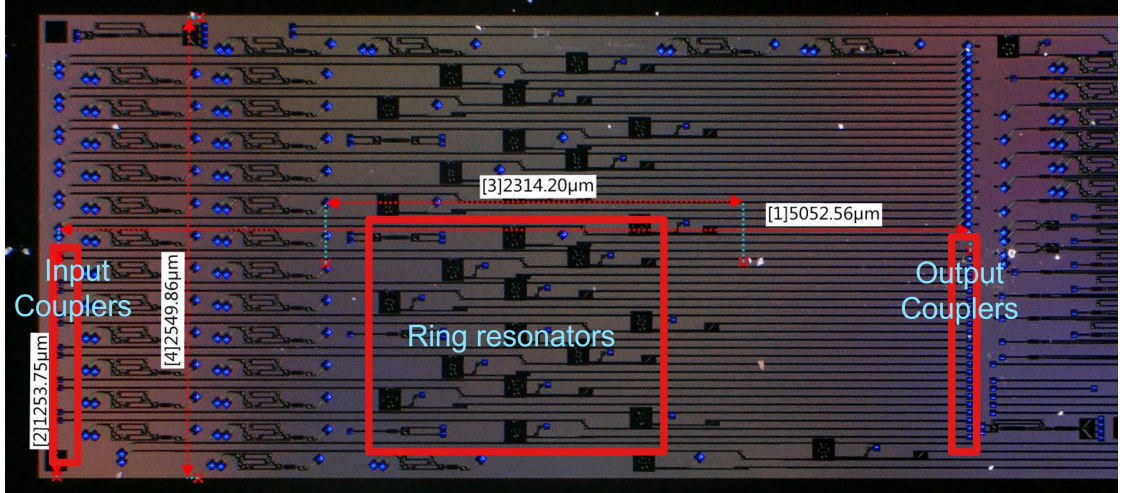

Figure 17: Micro structure dimensions of the test chip. The distance between the input and output couplers is 5052.56μm, the area arranged for the ring resonators is 2314.20μm $\times$ 1253.75μm.

because the arcylic channel can be made into different shapes to suit the chip. Because the channel size required in this project is larger, this solution can be simplified.

On the base of the arcylic channel method, we use 3D printing to fabricate the body of the
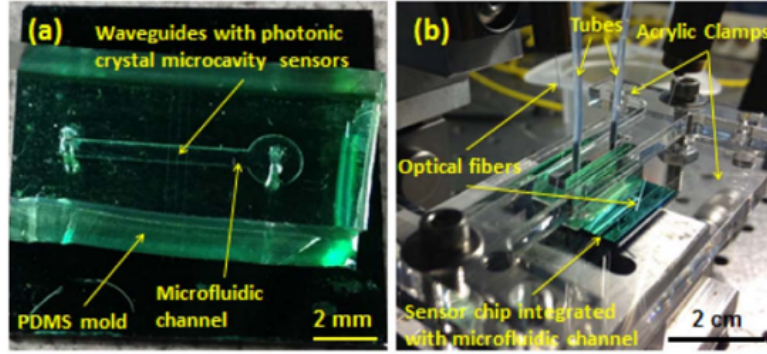
Figure 18: Microfluidic channel in experimental setup, which includes (a) a device with PDMS microfluidic channel and (b) the measurement setup. [14]
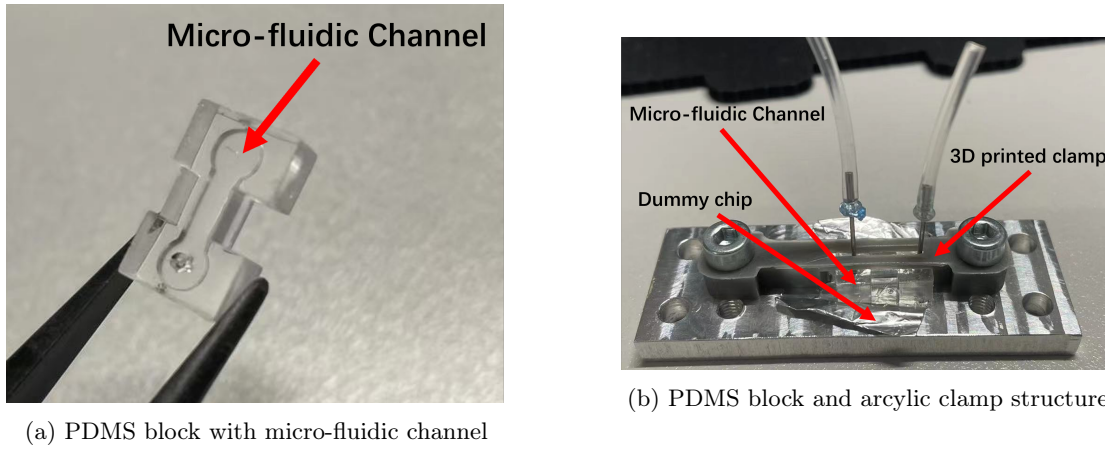

(a) PDMS block with micro-fluidic channel

(b) PDMS block and arcylic clamp structure

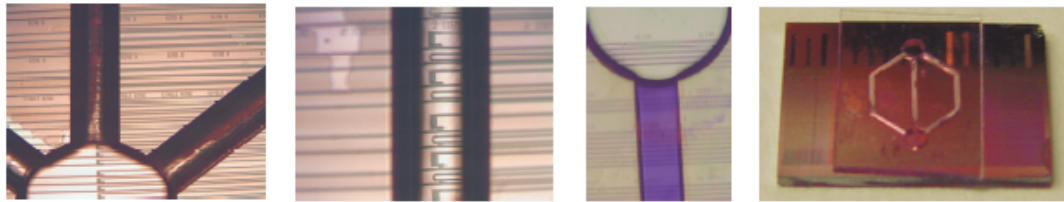Figure 19: Solution with PDMS block and 3D printed clamp.

Figure 20: Arcylic Microfluidic channel. From left to right are pictures of the channel taken under different scale. [3]

channel, and cover the bottom side of the channel with the PDMS sheet, which provides a deformable interface between channel and chip to protect the chip and seal the liquid. The PDMS sheet is glued with the 3D-printed channel by super glue.

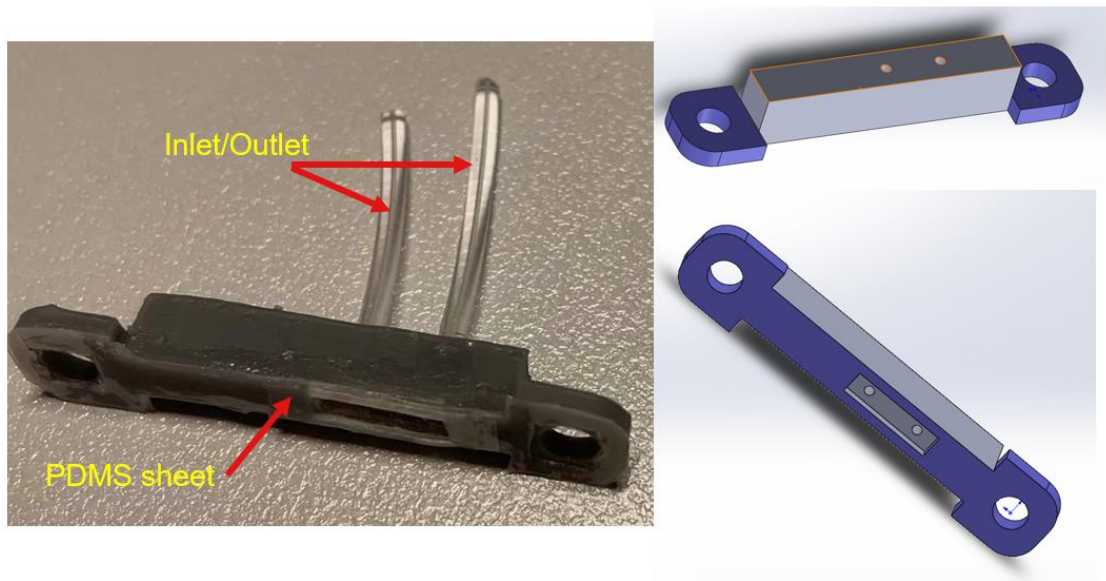To change the cladding of the ring resonators, we use a syringe to inject and suck liquid in the

Figure 21: The micro-fluidic channel and its 3D model in Solidworks. The micro-fluidic channel is formed by a 3D-printed body and PDMS sheet applied on the bottom. Note that there is an extra layer of PDMS sheet around the hollow to prevent leakage. Two tubes are inserted in the holes as the inlet and outlet of the liquid.
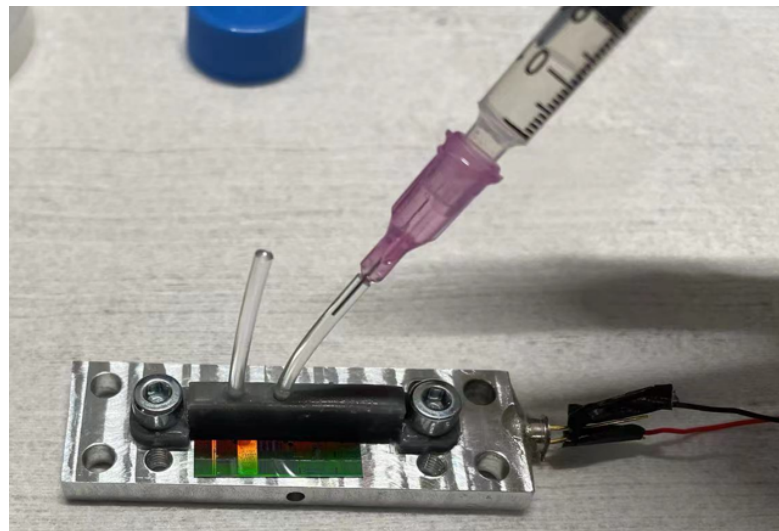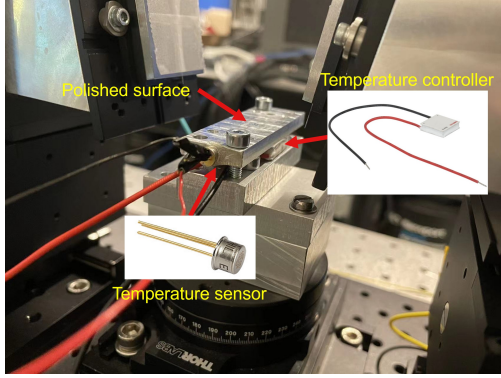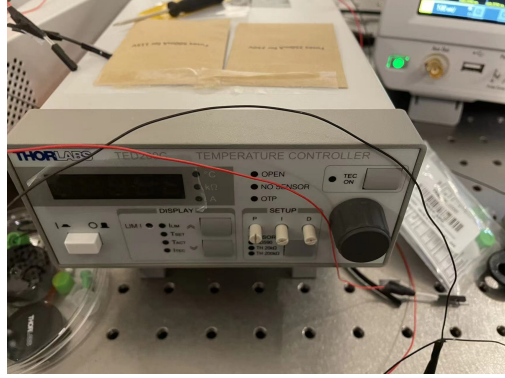

Figure 22: Change the liquid in the micro-fluidic channel. Liquid is injected with a syringe. After the channel is full-filled, extra liquid is collected on the other tube.

channel. As shown in Fig. 22, the liquid comes out from the outlet and can be removed.

(a) Temperature control system.

(b) Temperature controller TED200C.

Figure 23: Temperature control system and temperature controller.

4.3 Temperature Control

The temperature control system in this setup includes a temperature controller, a temperature transducer and an electric heater. The electric heater is a single stage thermoelectric cooler (TEC) element, we use TECF1S from THORLABS. This TEC element is attached under the chip holder plate to heat or cool the whole plate in a short time due to its low heat capacity. The temperature transducer, AD590 from THORLABS, is fixed on the side of the plate, sending the real-time temperature to the temperature controller, TED200C from THORLABS. With the controller, the target temperature can be easily set. After tuning the built-in PID control parameters in the controller, the feedback temperature control loop is built. The time constant of the temperature control is about 60 seconds.

4.4 Optical read-out

To collect experiment data, we use a Fiber Photodiode Power Sensor as shown in Fig. 24a and connect it to a Digital Optical Power and Energy Meter shown in Fig. 24b. The reading of the power meter is recorded by an Oscilloscope as shown in Fig. 24c. As the input light source (Fig. 25) is set to sweep from the wavelength of 1530 nm to 1620 nm, the spectrum can be displayed on the oscilloscope to show the intensity in this wavelength after setting the trigger of recording and sweep to the same button.

The parameters used in the data collections are: sweep speed 50 nm/s, record time 2.4 s, sample rate 833 k/s. The minimal wavelength unit can be calculated as:

$$minimal\ wavelength\ unit = \frac{sweep\ speed}{sample\ rate} = \frac{50nm}{833000} = 0.06pm \tag{24}$$

And the record time 2.4s is longer than the sweep time 1.8s. This data collection is feasible for this experiment requirement.

5 Result

In this section, the result of simulation and experiment are shown and compared.

19

(a) Fiber photodiode power sensor

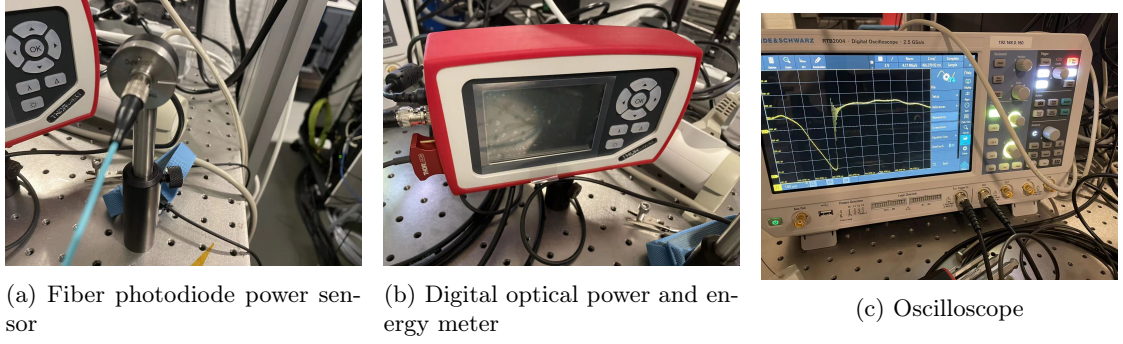(b) Digital optical power and energy meter

(c) Oscilloscope

Figure 24: Data collection devices.

Figure 25: Tunable input laser source with a tunable range of 1530nm to 1620nm.

5.1 Fluid control

Here we show some experimental results with fluid control.

Preparation of fluid samples   The specimens used in the experiments is prepared with a measuring cup and an electric scale with absolute error of 0.1g. Step are as following:

- Put the measuring cup on the scale, taring to zero point.
- Put chemical in the measuring cup with calculated amount and mix it with demineralized water. Take 10% NaCl solution as an example. Put 2g of NaCl in the measuring cup and add demineralized water until 20g. This would make NaCl solution with 10% mass concentration.
- Store the solution in a falcon tube with clear label on.

The result of different concentration of NaCl solution inside the micro-fluidic channel is shown in Fig. 26. The spectrum is around 1550nm and the intensities are normalized.

It can be observed that a red shift happens with the increasing concentration. The free spectrum ranges of the tips under different concentrations are very stable. We then take the local minimums
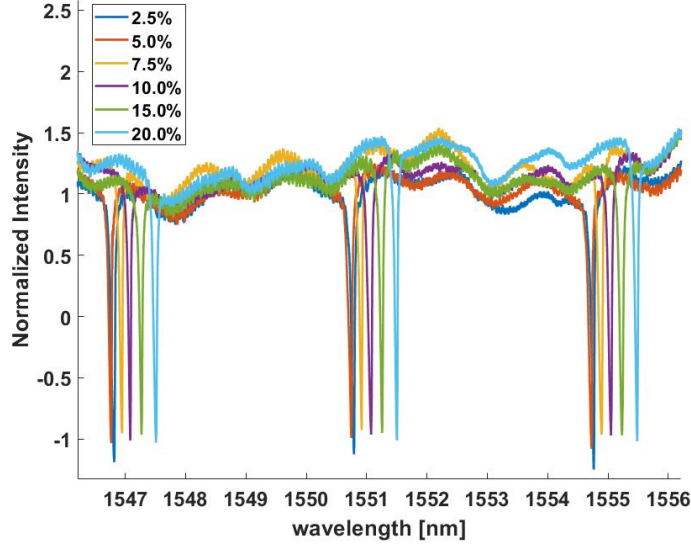
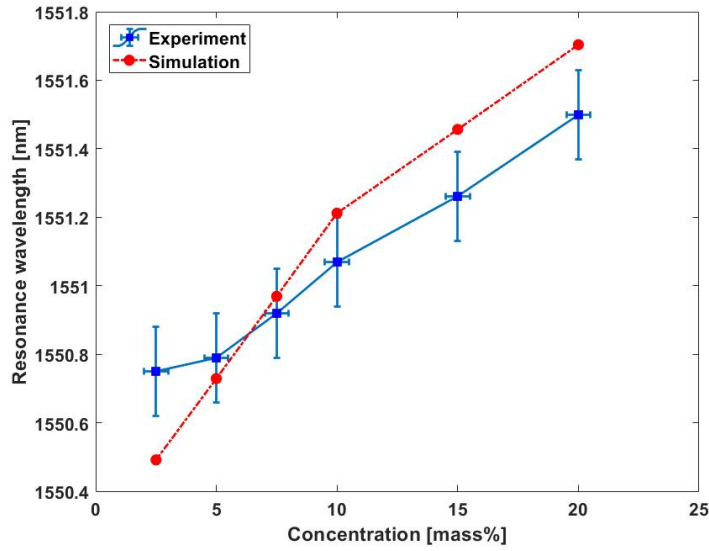Figure 26: Spectrum of NaCl solution under different concentrations.

Figure 27: Resonance wavelength of NaCl solution under different concentrations.

in the Fig. 26 as the resonance wavelength, and also the minimum before and after the chosen range, and compare the experiment data with the simulation result. The result is shown in Fig. 27. The slope of the curve after linear fitting is the sensitivity of the resonance wavelength with respect to the change of NaCl concentration as cladding.

The estimated error bars in this plot include the x error caused by error in weight and the y error
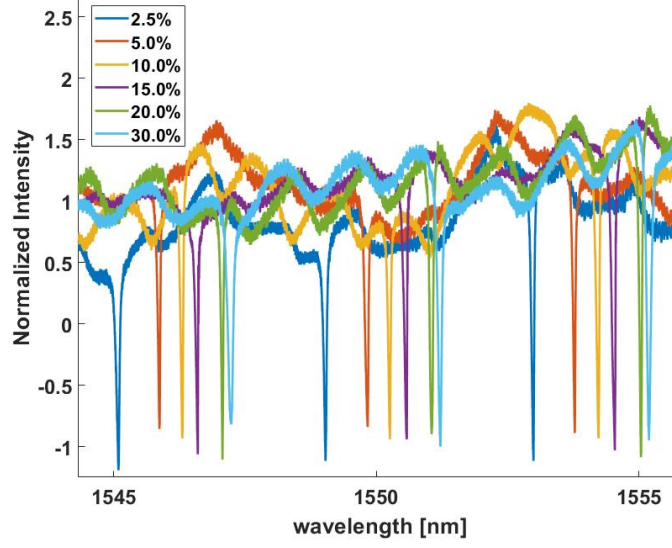
Figure 28: Spectrum of glucose solution under different concentrations.

caused by reading error and temperature instability. The sensitivity of resonance wavelength with respect to concentration is acquired with line fitting. The average sensitivity of three experiment groups around 1550nm is 0.04412nm/mass%, while the simulation result is 0.06854nm/mass%.

Similarly, the experiment result of glucose solution is shown in Fig. 28.

The glucose experiment also shows a similar red shift. We take the local minimums in the figure as the resonance wavelength, and also the minimum before and after the chosen range, and compare the experiment data with the simulation result. The result is shown in Fig. 29.

The estimated error bars in this plot are: x error caused by error in weight, y error caused by reading error and temperature instability. The sensitivity of resonance wavelength with respect to concentration is acquired with line fitting. Average sensitivity of three experiment groups around 1550nm is 0.07357nm/mass%, the simulation result is 0.04097nm/mass%.

5.2   Temperature control

With the temperature control system, we collect data under different temperatures to see the change in the resonance wavelength. The spectrum is shown in Fig. 30.

A red shift happens when temperature goes up. The resonance around 1550nm shows a different pattern with two tips, so we take the right tip as the data point. Similar with the method in Sec. 5.1 , the plot of temperature is shown in Fig. 31.

The sensitivity of resonance wavelength with respect to temperature is acquired with line fitting. The average sensitivity of three experiment groups around 1550nm is 0.0805nm/°C, the simulation result is 0.12nm/°C.
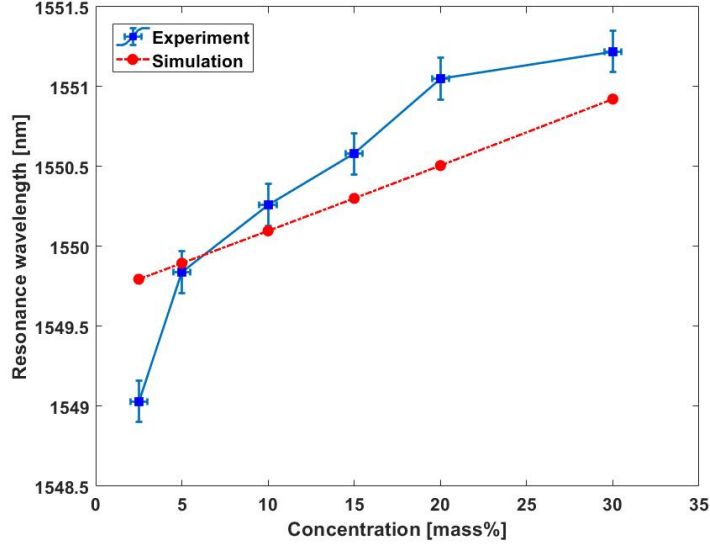
Figure 29: Resonance wavelength of glucose solution under different concentrations.
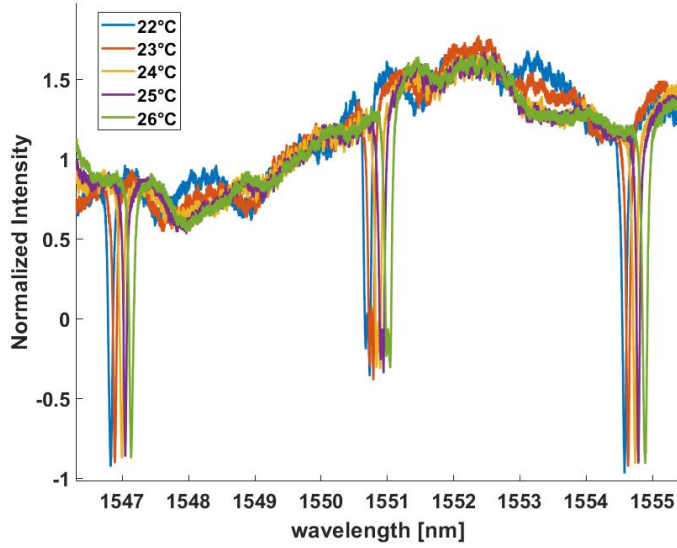

Figure 30: Spectrum under different temperatures.

5.3 Functional layer control

With the test chip being covered by a functional layer, it is able to sense certain biomarker with the receptors on the surface, because the binding between biomarker and receptor changes the effective refractive index of the SOI waveguide. We cover the surface of the test chip with functional layer and treat it into three different conditions, as shown in Fig. 15. These different
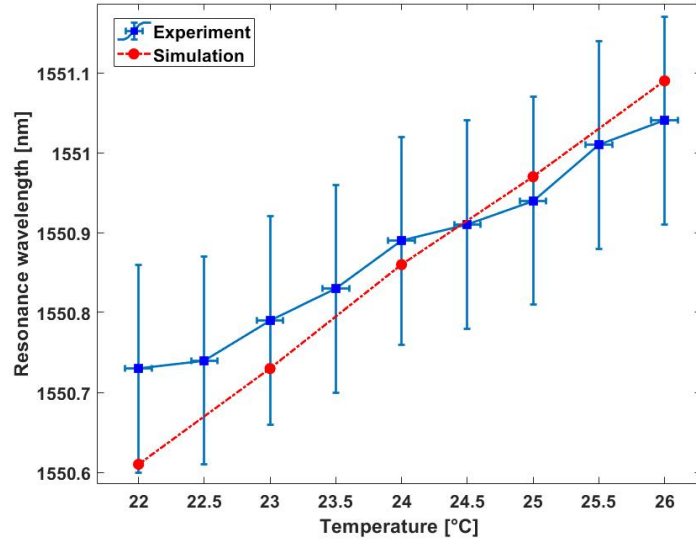
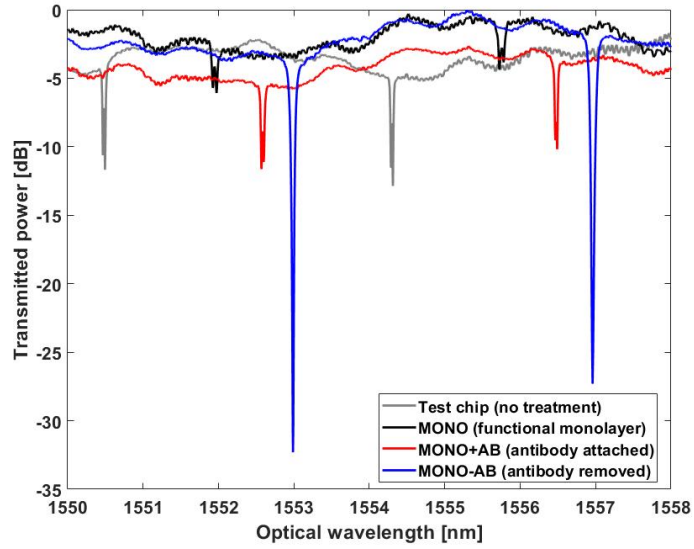Figure 31: Resonance wavelength under different temperatures.

Figure 32: Spectrum under different functional layer conditions.

conditions are simulated as different layer thicknesses in the simulation model. Bare chip (test chip) as 0nm, only monolayer (MONO) as 1.1nm, monolayer plus antibody (MONO+AB) as 1.9nm and monolayer minus antibody (MONO-AB) as 1.7nm. The test samples are treated by our collaborator in Wageningen University and Research. The experiment spectrum are shown in Fig. 32.
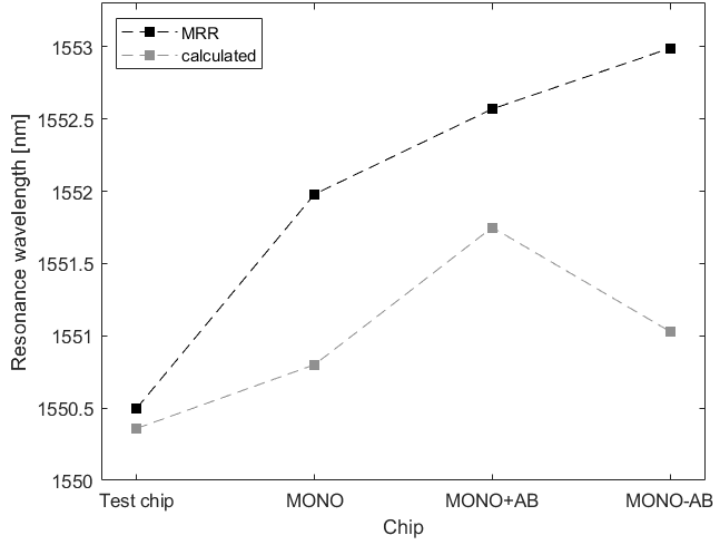
Figure 33: Resonance wavelength under different functional layer conditions.

The resonance wavelength of different layer thicknesses and the compare number in simulation is shown in Fig. 33.

5.4 Real-time treatment of chip with functional layer

Preparation of fluid samples The base solution in the experiment is 0.01 M phosphate buffer, 2.7 mM potassium chloride, 0.137 M sodium chloride, which also called PBS. 0.4 mM Tween is also added to the solution to maintain stability of the bounds between biomarkers and receptors. It is denoted as 0 concentration in the experiment. We choose protein HER2 as the target biomarker. And the solution of 50mM DL-Dithiothreitol (DTT) is also used to remove the protein as the last step in the experiment. The specimens used in the experiments is prepared with measuring cups, a pipette and an electric scale with absolute error of 0.0001g. Step are as following:

- Put a PBS tablet in the measuring cup, add 200mL of Demineralised water and wait for the tablet to dissolve completely.

- Add at most 0.1% by volume Tween, which is 0.2mL. This solution is the base solution in the following procedures.

- Mix 50mL base solution with 50μg of HER2 protein and make it into 1000ng/ml HER2 protein solution. This would be the solution to be diluted into samples with many other concentrations.

- Use a pipette to absorb certain amount of HER2 protein solution for a certain concentration. Take 0.08ng/ml sample as an example. Absorb 0.08 μl of the solution, put it in a measuring cup, and add the base solution until 10ml.

- Put a measuring cup on the electric scale, tare to zero point, and put 0.077g of DTT power in the cup. Then add base solution until 10ml. This would make 50mM DTT solution.
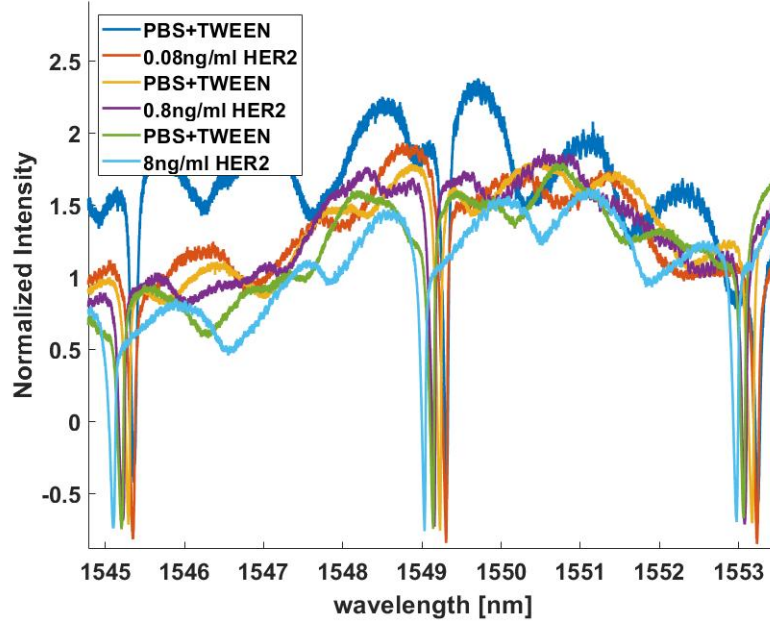
Figure 34: Spectrum of six experiment data with sample 1. Each curve on the figure shows the measurement result after a step of treatment. From top to bottom, the resonance wavelength shift to the left after every step. Here only shows six groups of data, the pattern is similar for all experiments for sample 1 and sample 2.

With the combination of temperature control and micro-fluidic channel, the experiment that make the biomarkers treat the functional layer in real-time is performed. We measure the resonance wavelength after guiding the protein solution through the micro-fluidic channel. The experiment is performed with temperature controlled at $22°C \pm 0.5°C$.

There are three samples to test in the experiment. Sample 1 and 2 have functionalized surface (hydrocarbons) with antibody (trastuzumab) that can bind with chosen HER2 protein, sample 3 has functional layer but without the antibody.

A part of the spectrum of sample 1 is show in Fig. 34. Sample 2 has a similar spectrum with sample 1. The resonance wavelength of each experiment is shown in Fig. 35 and Fig. 36.

As can see from the spectrum and the result, the resonance wavelength is shifting to the left side constantly. The shift of the resonance wavelength is recorded in Fig. 37a and Fig. 37b.

The spectrum of sample 3 is shown in Fig. 38, and the resonance wavelength of each experiment is shown in Fig. 39.

6 Discussion

Fabrication of the micro-fluidic channel   To prevent leakage of the fluid in the micro-fluidic channel, we apply an extra layer of PDMS sheet around the hollow in the channel. As shown in Fig. 40, this will add extra thickness around the seal and keep the liquid inside the hollow.
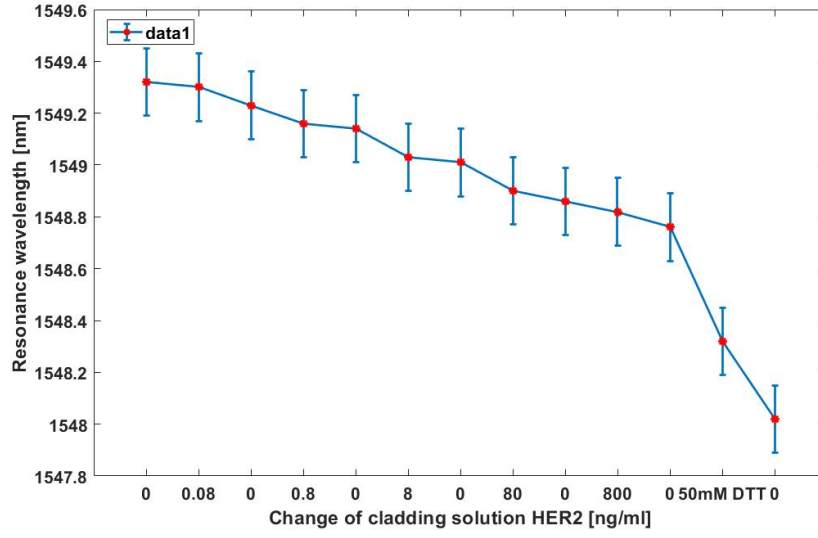
Figure 35: Resonance wavelength of each experiment with sample 1. The x axis is the concentration of HER2 protein in PBS+TWEEN base solution. Note that the point of 50mM has no HER2 protein.
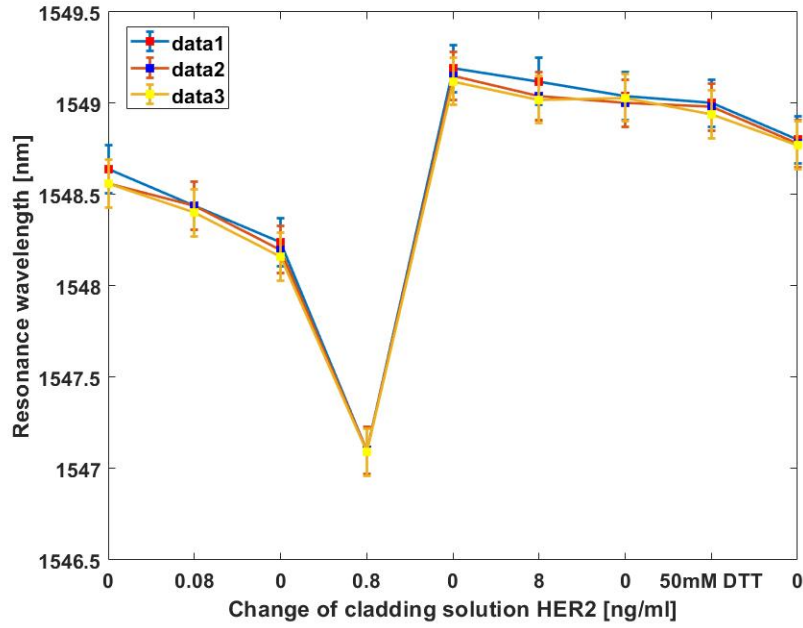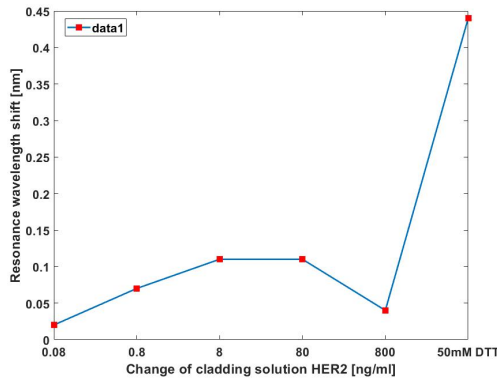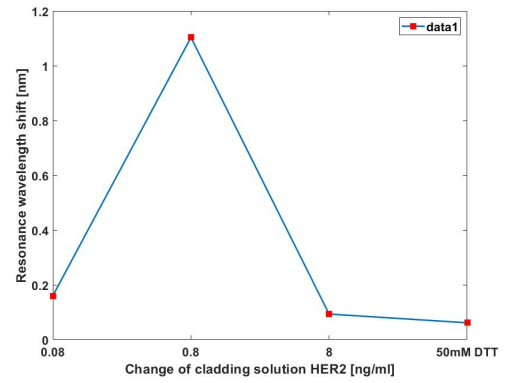

Figure 36: Resonance wavelength of each experiment with sample 2. Three data points are taken in this experiment. The x axis is the concentration of HER2 protein in PBS+TWEEN base solution. Note that the point of 50mM has no HER2 protein.

(a) Sample 1.   (b) Sample 2.

Figure 37: Resonance wavelength shift of each experiment with (a) sample 1 and (b) sample 2. The data points are calculated by extract the absolute difference between every zero concentration and the point after it.
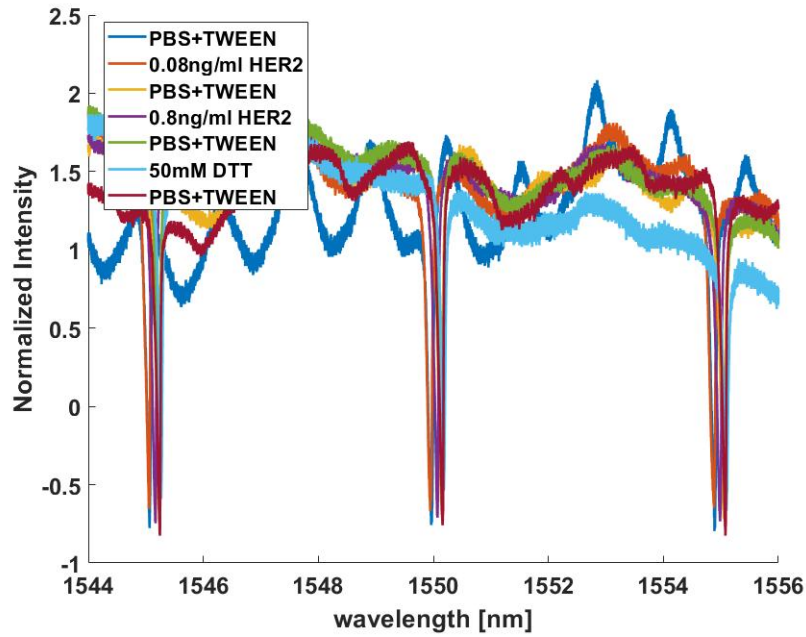
Figure 38: Spectrum of experiment data with sample 3. The movement pattern of the resonance wavelength is hard to find on the spectrum.

However, this extra thickness could also lead to more deformation in the 3D-printed body of the channel due to unequal stress applied on the part. As the part is repeatedly used, there is a higher chance for leakage to happen and the part could break.

To fix this flaw in our design, we can replace the PDMS sheet with a PDMS block with the same

Figure 39: Resonance wavelength of each experiment with sample 3. Obviously that the change of the resonance wavelength is very small and ramdom. The x axis is the concentration of HER2 protein in PBS+TWEEN base solution. Note that the point of 50mM has no HER2 protein.

Figure 40: Bottom view of the micro-fluidic channel. We use a big PDMS layer to cover the bottom surface, and apply an extra PDMS layer around the hollow to prevent leakage.
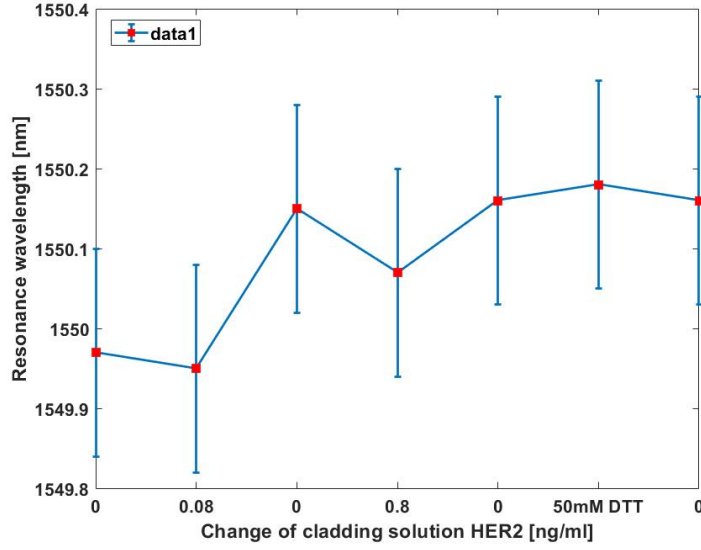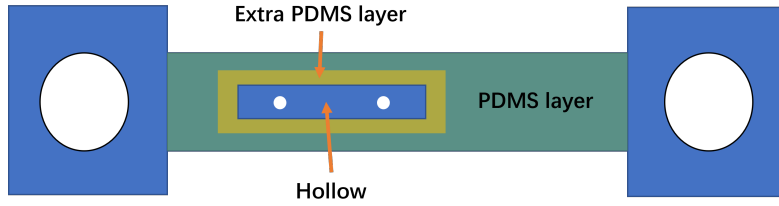
shape as the bottom of the channel. This PDMS block can be designed thicker than the PDMS sheet. With this change, we can fasten the screw with a larger force to seal the liquid without worrying about breaking the chip because of the large elasticity of the PDMS block. And the force can be distributed equally along the 3D-printed body to prevent sever deformation and part failure.

Assembly of the setup with the test chip Before the experiment, the test chip should be assembled with the setup properly. After putting the chip on the chip holder in the right direction, we align the micro-fluidic channel with the chip under a microscope. First, we roughly align the chip with the channel by eyeballing. Then, we fix both sides of the channel with screws, but do not fasten them. Next, we adjust the position of the chip carefully under the microscope until both sides of the optical couplers are exposed in the air. Last, we fasten the screws and check if the couplers are still reachable.

Because applying the micro-fluidic channel on the chip may influence the optical characteristics

29

of the chip, after the channel is aligned and fixed, we do not move it until a group of experiments are done to maintain a stable environment. If the channel is removed during the test, this effect should be considered in the result.

Fluid control To test the micro-fluidic system, we perform experiments with NaCl solution and glucose solution. By changing the cladding with solution of different concentration, we can observe a clear shift in the resonance wavelength. As Eq. 15 and Eq. 14 show, the refractive indices of both solution increase as the concentration rises . The red shift in the resonance wavelength also verifies this assumption.

After extracting the resonance wavelength of the experiment, we compare it to the simulation result. The sensitivity of NaCl experiment is about 35.6% less than simulation, and the sensitivity of glucose experiment is about 79.6% larger than simulation.

The deviation of the NaCl experiment could be caused by the error accumulation in the process. The deviation of the glucose experiment is much larger, and that could be caused by the concentration gradient, the concentration near bottom could be higher than average, which leads to a higher refractive index.

The experiment process of fluid control is done with a syringe to change the cladding solution, but the system can also handle continuous flow if we connect the syringe to a syringe pump.

Temperature control Experiment about the temperature control system is performed with bare chip, which can be treated as air cladding. With the temperature control system, we increase the temperature from room temperature 22°C by 0.5°C until 22°C, and record the spectrum at each step.

The resonance wavelength demonstrates a red shift when temperature increases. The result shows a relative linear curve. The sensitivity of experiment is about 32% less than the simulation result. The deviation is caused by the error in reading the data tip and temperature instability.

Functional layer control In this experiment, we use four chips that share the same geometry but treated with different processes, therefore the chips have different functional layer conditions as the cladding parameter. These different cladding are simulated as the same material layer but with different layer thicknesses.

The experiment result shows an increase in the resonance wavelength as the layer thickness rises. The simulation result shows an increased resonance wavelength in MONO and MONO+AB, but a decrease in MONO-AB because the layer thickness decreases. This difference between experiment and the simulation could be caused by the treatment of the surface being not as ideal as simulation. The process to remove the antibody should make the thickness thinner, but it could actually attach more thickness to the surface.

Real-time treatment of chip with functional layer Experiment of real-time treatment is performed in following steps. First, we inject the base solution and measure the resonance wavelength. Second, we inject the solution with protein and measure again. Then, we inject base solution again to wash away remaining protein and measure again. As this process takes about 5 minutes, and the wash away process cannot clean all protein in the solution, the resonance wavelength shift to the left when protein is added, and continue shifting after the washing process. The result is shown in Fig. 35.

The shift is caused by the bind of protein to the antibody on the chip surface. The shift between the first and the second data points is very small, which means 5 minutes is not sufficient for the device to detect the HER2 protein with a concentration of 0.08ng/ml. After that, the shift between the 0 concentration point and protein point is detectable and getting larger until the concentration is 80ng/ml, this showing that the shift is related with the biomarker concentration. The shift between 0 concentration point and 800ng/ml point is smaller than the last shift. This could be caused by the antibodies on the surface of the chip are mostly occupied and the binding efficiency also goes down. The result is shown in Fig. 37a.

Finally, the experiment with 50mM DTT is done with injecting DTT solution and wait for 10 minutes to let DTT do its work. The result shows that the shift still goes to the same direction.

Similar experiment is done with sample 2, as shown in Fig. 36. For sample 2, 3 measurement results are collected with a time gap of 1 minutes, and a very good data stability is shown on the figure. The result also shows a shift to the left, but a very large shift happens at 0.8ng/ml point, shown in Fig. 37b. This is because some accident happened in this step and the time of this step takes a very long time than last ones. As the protein has a longer time to bind with the antibodies on the chip, a large shift happens. After that, the shift goes to the right, this could be caused by some air bubble or other accident factor. And because the receptors on the chip are probably all occupied in last step, a very small shift is detected in the following measurements.

Sample 3 has no antibody to bind with the protein in the solution, so the result of sample 3 shows a random shift as expected, shown in Fig. 38 and Fig. 39. The shift of the resonance wavelength is mostly within the measurement error bar.

7 Conclusion

This project focuses on the examination for integrated photonic sensor. Starting from the basic properties of the photonic waveguide, the key property of the photonic sensor is the effective refractive index of the ring resonator. As the cladding environment, temperature and biomarker binding changes, the effective refractive index changes accordingly, leading to a shift in the resonance wavelength, which is the sensing principle of the sensor.

Based on the theory of the sensor, a simulation process is developed to predict the performance of the chip. The simulation is run in RSoft, where the geometry, material and other factors are defined. The results of simulation serve as a clear reference to the experiments.

To examine the performance of the sensor, a stable and robust experimental setup is built, including the alignment system, data collection devices, temperature control system and micro-fluidic system. Several factor control experiments are done with a test chip in this setup. Though some experiment results show large deviation when compared with the simulation, it still shows a promising pattern in the spectrum. The setup can also be be tailored easily to fit other different photonic chip with different structures.

For future work, it could be an interesting improvement to develop an integrated system, which can be designed to have heater inside the micro-fluidic channel to achieve better temperature stability. The micro-fluidic channel can also be designed with slots to have a better liquid sealing ability, and can be aligned with the chip more easily.

References

[1] Y. Chen, F. Yu, C. Yang, J. Song, L. Tang, M. Li, and J.-J. He. Label-free biosensing using cascaded double-microring resonators integrated with microfluidic channels. *Optics Communications*, 344:129–133, 2015.

[2] K. De Vos. *Label-Free Silicon Photonics Biosensor Platform withMicroring Resonators.* PhD thesis, Ghent University, 2010.

[3] K. De Vos, J. Girones, S. Popelka, E. Schacht, R. Baets, and P. Bienstman. Soi optical microring resonator with poly (ethylene glycol) polymer brush for label-free biosensor applications. *Biosensors and Bioelectronics*, 24(8):2528–2533, 2009.

[4] J. T. Kindt and R. C. Bailey. Biomolecular analysis with microring resonators: applications in multiplexed diagnostics and interaction screening. *Current opinion in chemical biology*, 17(5):818–826, 2013.

[5] J. Komma, C. Schwarz, G. Hofmann, D. Heinert, and R. Nawrodt. Thermo-optic coefficient of silicon at 1550 nm and cryogenic temperatures. *Applied Physics Letters*, 101(4):041905, 2012.

[6] A. Malinin, A. Zanishevskaia, V. Tuchin, J. Y. Skibina, and I. Silokhin. Photonic crystal fibers for food quality analysis. *Proc SPIE*, 8427:87–, 05 2012. doi: 10.1117/12.924096.

[7] J. S. Penadés, C. Alonso-Ramos, A. Khokhar, M. Nedeljkovic, L. Boodhoo, A. Ortega-Moñux, I. Molina-Fernández, P. Cheben, and G. Mashanovich. Suspended soi waveguide with sub-wavelength grating cladding for mid-infrared. *Optics letters*, 39(19):5661–5664, 2014.

[8] A. J. Qavi and R. C. Bailey. Multiplexed detection and label-free quantitation of micrornas using arrays of silicon photonic microring resonators. *Angewandte Chemie International Edition*, 49(27):4608–4611, 2010.

[9] G. T. Reed and A. P. Knights. *Silicon photonics: an introduction.* John Wiley & Sons, 2004.

[10] N. Rouger, L. Chrostowski, and R. Vafaei. Temperature effects on silicon-on-insulator (soi) racetrack resonators: A coupled analytic and 2-d finite difference approach. *Journal of Lightwave Technology*, 28(9):1380–1391, 2010.

[11] O. Scheler, J. T. Kindt, A. J. Qavi, L. Kaplinski, B. Glynn, T. Barry, A. Kurg, and R. C. Bailey. Label-free, multiplexed detection of bacterial tmrna using silicon photonic microring resonators. *Biosensors and Bioelectronics*, 36(1):56–61, 2012.

[12] L. Sun, J. Yuan, T. Ma, X. Sang, B. Yan, K. Wang, and C. Yu. Design and optimization of silicon concentric dual-microring resonators for refractive index sensing. *Optics Communications*, 395:212–216, 2017. ISSN 0030-4018. doi: https://doi.org/10.1016/j.optcom.2016.05.052. URL https://www.sciencedirect.com/science/article/pii/S003040181630414X. Nano-Optoelectronics: Advanced Optoelectronic Devices Based on Nanostructures and Nanomaterials.

[13] J. D. Suter, I. M. White, H. Zhu, H. Shi, C. W. Caldwell, and X. Fan. Label-free quantitative dna detection using the liquid core optical ring resonator. *Biosensors and Bioelectronics*, 23 (7):1003–1009, 2008.

[14] Z. Wang, H. Yan, S. Chakravarty, H. Subbaraman, X. Xu, D. Fan, A. X. Wang, and R. T. Chen. Microfluidic channels with ultralow-loss waveguide crossings for various chip-

integrated photonic sensors. *Optics letters*, 40(7):1563–1566, 2015.

[15] W. J. Westerveld and H. P. Urbach. *Silicon Photonics*. IOP Publishing, 2017.

[16] D.-X. Xu, M. Vachon, A. Densmore, R. Ma, S. Janz, A. Delâge, J. Lapointe, P. Cheben, J. Schmid, E. Post, et al. Real-time cancellation of temperature induced resonance shifts in soi wire waveguide ring resonator label-free biosensor arrays. *Optics express*, 18(22): 22867–22879, 2010.